Soft Matter

COMMUNICATION

View Article Online
View Journal

Spatial organization of surface nanobubbles and its implications in their formation process

Cite this: DOI: 10.1039/c3sm52724g

Henri Lhuissier,[a] Detlef Lohse[a] and Xuehua Zhang[b]

Received 25th October 2013
Accepted 2nd December 2013

DOI: 10.1039/c3sm52724g

www.rsc.org/softmatter

We study the size and spatial distribution of surface nanobubbles formed by the solvent exchange method to gain insight into the mechanism of their formation. The analysis of Atomic Force Microscopy (AFM) images of nanobubbles formed on a hydrophobic surface reveals that the nanobubbles are not randomly located, which we attribute to the role of the history of nucleation during the formation. Moreover, the size of each nanobubble is found to be strongly correlated with the area of the bubble-depleted zone around it. The precise correlation suggests that the nanobubbles grow by diffusion of the gas from the bulk rather than by diffusion of the gas adsorbed on the surface. Lastly, the size distribution of the nanobubbles is found to be well described by a log-normal distribution.

Nano- or micro-gas bubbles often form on hydrophobic solid surfaces which are in contact with an aqueous environment.[1–5] Their presence has been supported by many experiments, including measurements by attenuated total reflectance infrared, surface plasmon resonance[6,7] and quartz crystal microbalance.[8] At the scale of a single bubble, compelling evidence also comes from scanning transmission soft X-ray microscopy[9] and atomic force microscopy (AFM) imaging combined with the bubble response to ultrasound,[10] degassing[11] and pressure reduction.[12] Micro- and nanobubbles have significant implications for many interfacial processes, such as catalysis, drag reduction, biomolecular adsorption and surface erosion,[13–20] which have drawn attention for intensive research to understand their formation and stability mechanism.

Nanobubbles can be efficiently produced by the solvent exchange protocol.[21] This protocol consists of, first, covering the surface with gas saturated short-chain alcohol and, second, replacing the alcohol by water without drying the surface in between. Its efficiency may be attributed to the transient and local gas supersaturation close to the surface, when the alcohol, having a high gas solubility, is replaced by water, having a lower gas solubility. This local supersaturation presumably triggers the nucleation of small gaseous domains, the nanobubbles. The full dynamics of formation is thought to be faster than a few seconds.[22]

However, the mechanisms behind the nucleation and growth of the nanobubbles and the parameters controlling their size and number density remain unclear. The liquid environment during the solvent exchange precludes the possibility of monitoring the bubble formation by many techniques, including AFM. In order to gain insight into this dynamics of formation, we choose here a different approach: combining AFM imaging with statistical physics, we analyze the *terminal* (day-lasting) situation, namely the spatial and size distributions of the nanobubbles and the possible correlations between them, and draw conclusions on the formation process from the obtained statistics. This approach relies on the reported fact that, although the stability mechanism itself, which we will not discuss here, is yet unsolved,[23–26] once formed, the nanobubbles can be stable for a long period. In a previous analysis by Borkent *et al.*, the nanobubbles were found to have either a preferred radius of 20 nm or two separated preferred radii,[27] but the bubble size distribution was dependent on the bubble generation method and the correlation between the bubble sizes and distances was not studied. We use here Voronoi partitions of the surface around the nanobubbles, as already used in other contexts in which spatial self-organization plays a role,[28,29] especially in which growth and nucleation might compete,[30–32] in studying this correlation and drawing conclusions on the bubble formation mechanism.

The nanobubbles were formed on a smooth hydrophobic substrate (a silicon wafer coated with a self-assembled monolayer of octadecyltrichlorosilane by following the protocol in the literature[7]) by the standard solvent exchange method. The substrate surface was first covered by distilled ethanol saturated with air at ambient temperature. The ethanol was then replaced

[a]Department of Science and Technology, J. M. Burgers Center for Fluid Dynamics and MESA+, University of Twente, P.O. Box 217, 7500 AE Enschede, The Netherlands. E-mail: h.lhuissier@utwente.nl; d.lohse@utwente.nl

[b]Department of Chemical and Biomolecular Engineering and School of Chemistry, University of Melbourne, Parkville, VIC 3010, Australia. E-mail: xuehuaz@unimelb.edu.au

by water without being exposed to air.† After the solvent exchange, the surface was imaged by AFM in tapping mode (MFP 3D, Asylum Research) to obtain the topography of the bubbles. On a large scale (typically 100 μm), the surface density of nanobubbles varied strongly between 0 and more than 100 μm^{-2}, as already reported in various publications,[3–5,33] often presumably due to spatial variations in the mixing flow on this scale. We randomly chose areas among those having a large bubble density (from 10^{-2} to 100 μm^{-2}) and scanned them. Each scan covers a square area ranging from 8×8 μm^2 to 50×50 μm^2 with a lateral resolution of 1/512th of the square width, *i.e.* 6 to 98 nm.

In order to measure the bubble footprint area a and the bubble-depleted area around each bubble (see Fig. 1), the images were analyzed with a robust image processing code (Matlab) whose results were manually checked. The depleted areas were computed from a tessellation of the surface with each cell containing a single bubble.‡ Two different tessellations, resulting in two different measurements of the areas, were performed:

• The first one is the standard Voronoi diagram based on the distances to the bubbles' centers: a cell, with area A_{vor}, contains all and only those points of the surface which are closer to the center of a given bubble than to any other bubble's center (see Fig. 1(a)).

• The second one, that we call *modified* Voronoi diagram (also known as Appolonius diagram), is based on the distance to the triple contact lines, *i.e.* boundaries, of the bubbles: a cell, with area A, contains all and only those points of the surface which are closer to the *boundary* of a given bubble than to any other bubble's *boundary* (see Fig. 1(b)).

The second definition is identical to the first one only if all the bubbles have the same size. Otherwise, the modified cells are larger (resp. smaller) for the largest (resp. smallest) bubbles compared to the standard diagram. Our statistical analysis is based on the measurements of more than 1400 bubbles from 6 images collected in different experiments. In these experiments, the temperature of the liquids and substrate, the gas saturation of the liquids, and the fluid cell geometry, which influences the mixing pattern, were similar. We however note that the rate of replacement of ethanol by water was not controlled, which might influence the local gas saturation close to the surface, and with it nanobubble nucleation.

The obtained statistics reveals important characteristics about the spatial distribution of the nanobubbles. First, the bubbles' centers are not randomly distributed. Fig. 2 shows the probability distribution function (pdf) of the normalized area $A_{vor}/\langle A_{vor}\rangle$ of the cells, where $\langle A_{vor}\rangle$ represents the average area over the image, together with the normalized gamma distribution

$$p(x) = \frac{343}{15}\sqrt{\frac{7}{2\pi}}x^{5/2}e^{-7x/2}, \quad (1)$$

which is expected[34] in the case of a random Poisson process of nucleation, where all the bubbles would appear at the same time§. It shows that the experimental distribution is much broader than the gamma distribution, as corroborated by their respective standard deviations 1.23 and 0.53 (the latter value is an analytical derivation[35]). This means that the largest (resp. smallest) cells are larger (resp. smaller), with respect to the mean, than expected from a Poisson process.

This observation cannot be explained by discrete chemical or mechanical heterogeneities of the substrate's surface, since the heterogeneities themselves would be expected to be randomly distributed and would therefore also generate distribution (1). It can also not be explained by the mixing dynamics of the solvents generating transient gradients in gas supersaturation which would influence the distribution of A_{vor}, since the typical length scale expected for the gas concentration fluctuations $\sqrt{D/\dot{\gamma}} \sim 30$ μm, where $D \sim 10^{-7}$ m^2 s^{-1} and $\dot{\gamma} \sim 10^2$ s^{-1} respectively stand for the diffusivity of ethanol in water and the typical shear rate during the exchange, is much larger than the typical distance of 1 μm observed between bubbles of different

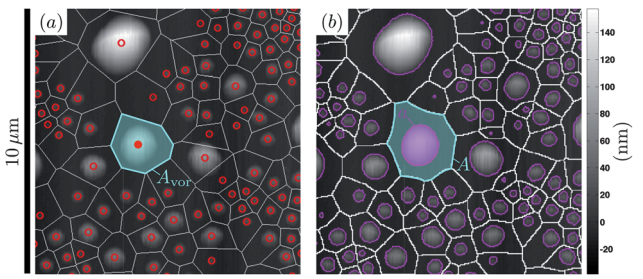

Fig. 1 Portion of a typical AFM image of the nanobubbles with the cellular diagram around the bubbles (white lines). (a) Voronoi diagram based on the distances to the bubbles' centers (red circles). One Voronoi cell (cyan), associated with the bubble center marked as a filled red circle, is shown. It has an area A_{vor}. (b) *Modified* Voronoi diagram based on the distance to the bubbles' triple contact lines (pink lines). One *modified* Voronoi cell (cyan), associated with the bubble footprint colored in pink, is shown. The bubble footprint has an area a, the cell has an area A.

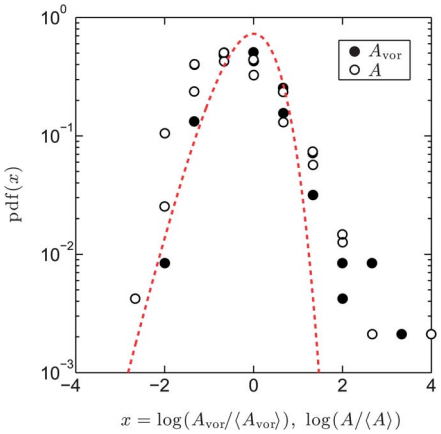

Fig. 2 Normalized pdf of the Voronoi cell areas A_{vor} (*cf.* Fig. 1(a)) and A (*cf.* Fig. 1(b)) around the nanobubbles (circles). The dashed line shows the distribution $p(x)$ from eqn (1) which would be expected for $A_{vor}/\langle A_{vor}\rangle$ in the case of a random spatial distribution of the nanobubbles. $\langle\cdot\rangle$ denotes the average value over each AFM image. The experimental pdf is much broader than a random spatial distribution.

sizes. We rather think that the extra-broadness of the experimental distribution in Fig. 2 (as compared to eqn (1)) results from the history of the nucleation process. During their formation, the growth of the bubbles already nucleated competes with the nucleation of new bubbles: if some bubbles nucleate and start growing before (resp. after) the others, they are likely to reach much larger (resp. smaller) relative sizes than in the case where all bubbles would nucleate at the same time. This qualitative explanation for the extra-broadness of the distribution is also consistent with Gilbert's[35] mathematical demonstration that a Poisson nucleation process which is random both in time and space increases the standard deviation, *i.e.* broadens the distribution, as compared to eqn (1), which corresponds to a process random in space only.

Besides the precise mechanisms of nucleation and growth at play, we observe that the departure from a random location of the bubbles is clearly related to the variation in their individual sizes. Fig. 3 shows the normalized size of the Voronoi cells $A_{vor}/\langle A_{vor}\rangle$ *versus* the normalized size of the bubbles $a/\langle a\rangle$. It is clear from the plot that small bubbles (as compared to the mean) can have small or large depleted areas, whereas large bubbles can only have large depleted areas. This is also noticeable in Fig. 1(a), where small (resp. large) bubbles typically have large (resp. small) depleted areas, except for those small bubbles which are next to large bubbles. Note that this correlation is not *a priori* obvious: for the standard Voronoi diagram, the area of the cells only depends on the locations of the bubbles' centers, not on their sizes (this is why we plot A_{vor} and not A in Fig. 3). Fig. 3 therefore demonstrates that the bubbles' sizes and relative locations are indeed correlated.

In order to understand this correlation between size and relative locations, it is actually not relevant to consider the standard Voronoi diagram. Indeed, if one thinks about the depleted zone as the zone from which the bubbles took the gas required for their growth, an equal distance from the bubbles' boundaries, where the gas escapes the solution, seems to be a better criterion than an equal distance from the bubbles' centers to distinguish between the bubble-depleted areas of neighboring bubbles. The inappropriateness of the standard Voronoi diagram for the definition of the depleted areas is also obvious in Fig. 1(a), where some bubbles extend outside their own cell.

We therefore consider now only the *modified* Voronoi diagram and the associated cell areas A. Fig. 4 shows the absolute areas A *versus* the corresponding absolute bubbles' footprint areas a. The areas extend over more than four decades and it is clear that large bubbles have large cells and *vice versa*. This shows a new important point with respect to the normalized values of Fig. 3: not only at the scale of each image, but also for different images, are the size and relative location of the bubbles strongly correlated. We emphasize that this correlation holds for all the images, which were all chosen among the areas with the largest surface density of nanobubbles, but from different experiments where the rates of mixing were not necessarily the same. This suggests a universal mechanism for the formation of nanobubbles by solvent exchange.

The data in Fig. 4 can be quantitatively understood from a model assuming that the bubbles grow by absorbing the gas contained in the *bulk* liquid around them. Indeed, assuming a gas-depleted volume around the bubbles which is roughly hemispherical, *i.e.* typically as thick (perpendicular to the surface) as it is wide (along the surface), and a uniform gas supersaturation yields $N = c\Omega_A$ for the number of gas molecules above saturation which where initially enclosed in the cell volume $\Omega_A \equiv \alpha_A A^{3/2}$ having the shape of a hemisphere with section A, where c is the gas concentration above saturation and α_A is a geometrical factor.¶ If all these molecules collect into the bubble at the center of the cell, and assuming a contact angle θ independent of the bubble size, one also has $N = p\Omega_a/kT$, where p, $\Omega_a = \alpha_a a^{3/2}$,¶ k and T respectively stand for the pressure in the bubble, the bubble volume, the Boltzmann constant and the temperature. The pressure in the bubble being the sum of the ambient pressure p_a and the Laplace pressure $2\sqrt{\pi}\sin\theta\sigma/\sqrt{a}$

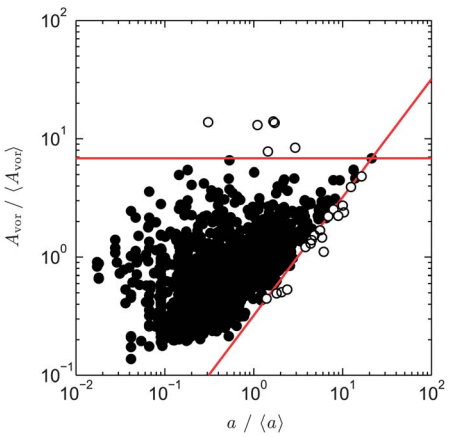

Fig. 3 Normalized Voronoi cell area $A_{vor}/\langle A_{vor}\rangle$ *versus* normalized nanobubble footprint area $a/\langle a\rangle$. More than 98% of the bubbles measurements (filled circles) lie between the two lines $y \propto x$ and $y =$ const intersecting at the point with the largest measured $a/\langle a\rangle$. The bubbles outside these lines are marked with open circles.

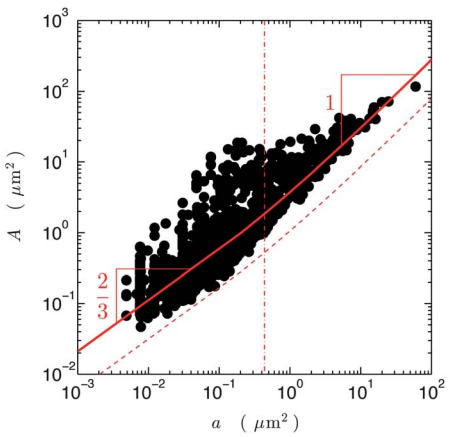

Fig. 4 Area A of the *modified* Voronoi cells *versus* the area a of the nanobubble footprints (filled circles). The dashed and plain lines show eqn (2) with $c = 6.1$ and 0.9 mol m^{-3}, respectively. The vertical dash-dotted line shows the transition between small and large bubbles.

(due to the bubble interface's curvature, and therefore depending on the bubble size a), equating the two aforementioned expressions for N yields

$$A = \left[\frac{1}{kTc}\frac{\alpha_a}{\alpha_A}\left(p_a + 2\sqrt{\pi}\sin\theta\frac{\sigma}{\sqrt{a}}\right)\right]^{2/3} a. \quad (2)$$

Eqn (2) is compared to all our data, coming from different images, in Fig. 4. The dashed line uses the difference of the air concentrations at saturation in ethanol and water for c,[36,37] *i.e.* $c \simeq 6.1$ mol m^{-3} and $\theta = 165°$.[38–40] This value of c overestimates the actual supersaturation during the solvent exchange, since obviously not all the gas dissolved in ethanol will dissolve in water. We therefore also plot eqn (2) with $c = 0.9$ mol m^{-3} (solid line), the value providing the best fit to the data. It follows the data over the four decades of the measurements. Note that the first assumption in our model is not exactly satisfied since the bubbles grow isotropically only until they start interacting with each other. We however think that the distortion from sphericity cancels on average and is only responsible for the (asymmetric) dispersion around eqn (2) (which we already discussed based on Fig. 3). We also think that constant gas supersaturation and contact angle are the most reasonable assumptions since, as already mentioned, the gas content of the ethanol was always the same in the experiments and we only analyzed the areas with the largest bubble density, and under the same conditions, the contact angles of neighboring nanobubbles are reported to be equal within a few degrees.[38–40]

Table 1 shows the limiting scaling relationships between a and A for the volume-growth scenario leading to eqn (2) (right column), and in addition the alternative relationships (left column) that would have been expected if the bubbles had grown by absorbing the gas adsorbed on the surface around them, rather than the gas contained in the *bulk* liquid around them (as our model assumes). This alternative scenario (surface growth) can clearly be discarded on the bases of Fig. 4.

Lastly, Fig. 5 shows the pdf of the bubble size. It is found to be well fitted by a log-normal distribution

$$q(x) = \frac{1}{\sqrt{2\pi}sx}\exp\left[-\frac{1}{2}\left(\frac{\ln x + s^2/2}{s}\right)^2\right], \quad (3)$$

with the same standard deviation $s = 1.10$ as the experimental data. The physical reason behind this distribution is unclear to us. Log-normal distributions naturally arise in sequential fragmentation processes.[41] They have in particular been observed for the size of the plumes in buoyancy driven turbulent flow,[42,43] as a consequence of the repeated breakage of the largest plumes into smaller and smaller structures. However, a similar scenario

Table 1 Expected relationships between a and A for small ($a \ll a_c = 4\pi \sin^2\theta\sigma^2/p_a^2 \simeq 0.44$ μm^2) and large ($a \ll a_c$) bubbles in the case of diffusive growth from the surface area A or from the volume $\propto A^{3/2}$

	Surface growth	Volume growth
Small bubbles	$A \propto a$	$A \propto a^{2/3}$
Large bubbles	$A \propto a^{3/2}$	$A \propto a$

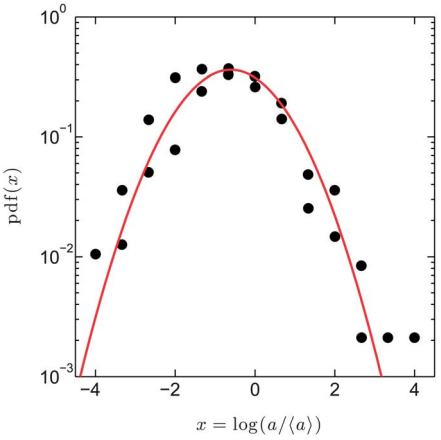

Fig. 5 Normalized pdf of the normalized nanobubble footprint area $a/\langle a\rangle$ (filled circles). The line shows the log-normal distribution $q(x)$ from eqn (3) with the same standard deviation of the logarithm $s = 1.10$ as the measurements.

producing smaller and smaller structures of gas-rich regions down to the scale of the nanobubbles is clearly unexpected, since the smallest size of gas concentration fluctuations $\sqrt{D/\dot{\gamma}}$ is much larger than the typical distances $\sqrt{A}$ between the bubbles, as already discussed above. Log-normal distributions have also been reported in another nucleation driven process: for the grain sizes in the re-crystallization of metallic melts,[44] but, as far as we know, no physical justification of this observation has been given.

In summary, the statistical study of the size and spatial location of surface nanobubbles proved to be an efficient tool for obtaining information on the mechanism of formation of the nanobubbles. Nanobubbles' centers are not randomly distributed, which means that nanobubbles do interact during nucleation and growth. The size of each nanobubble is strongly correlated with its distances from the closest neighboring nanobubbles. This shows that nanobubbles grow by gas depletion of their surroundings. The precise correlation actually suggests that the growth is driven by gas diffusion from the bulk rather than diffusion from the gas adsorbed on the surface. The study also yielded the size distribution of the nanobubbles, whose physical origin however remains unclear to us. Obtaining more insight into this process will require to understand the rates of nucleation of nanobubbles, which might also shed light on the yet unknown mechanism behind their remarkable stability against dissolution.

Acknowledgements

We gratefully acknowledge various discussions with Chao Sun and Harold Zandvliet, and financial support by ERC under an advanced grant.

Notes and references

† The pretreatment of water before use was important for reproducibility. Filtered Milli-Q water by Millipore was first stored at 4 °C overnight, and before use, a

small vial of cool water was warmed up to 30–35 °C, and used immediately. To avoid contamination, glass syringes and metal needles were used instead of plastic or one-use syringes or needles. The AFM cantilever was cleaned by exposure to UV/ozone for 15 minutes and the AFM measurements were conducted under ambient conditions.

‡ The background of each image was subtracted and the bubbles were detected by applying a threshold in the height above the local background level. The bubble area a was measured from the number of pixels detected in each bubble and its center computed as the barycenter of these pixels. The results of the processing were individually checked: all and only those bubbles that could be seen on the images were detected. We also checked that the area a was essentially independent of the threshold, around the value we used. The measurements of the bubble-depleted areas imply that the whole neighborhood of each bubble is analyzed. These requirements can obviously not be fulfilled close to the borders of the images. We therefore considered only those bubbles, the center of which lies inside a central square with 64% of the area of the full image (we checked that this yields only valid cell area measurements).

§ Although eqn (1) is not an analytical result but a fit to numerical results with the same form as the analytical result to the one-dimensional case, it is accurate enough for our present concern.[34]

¶ The geometrical factors α_a and α_A depend on the volume shapes through the function $f(\theta) = \frac{4}{3\sqrt{\pi}} \frac{(2-\cos\theta)\cos^4(\theta/2)}{\sin^3\theta}$. For a hemispherical gas-depleted volume $\mathcal{Q}_A$ and a bubble volume $\mathcal{Q}_a$ with a spherical cap shape with contact angle in the gas phase $180° - \theta \simeq 15°$, one has $\alpha_a/\alpha_A \simeq 0.10$

1 H. K. Christenson and P. M. Claesson, *Adv. Colloid Interface Sci.*, 2001, **91**, 391–436.
2 P. Attard, *Adv. Colloid Interface Sci.*, 2003, **104**, 75–91.
3 J. R. T. Seddon and D. Lohse, *J. Phys.: Condens. Matter*, 2011, **23**, 133001.
4 V. S. J. Craig, *Soft Matter*, 2010, **7**, 40.
5 M. A. Hampton and A. V. Nguyen, *Adv. Colloid Interface Sci.*, 2010, **154**, 30–55.
6 X. Zhang, A. Khan and W. Ducker, *Phys. Rev. Lett.*, 2007, **98**, 136101.
7 X. Zhang, A. Quinn and W. A. Ducker, *Langmuir*, 2008, **24**, 4756–4764.
8 X. Zhang, *Phys. Chem. Chem. Phys.*, 2008, **10**, 6842.
9 L. Zhang, B. Zhao, L. Xue, Z. Guo, Y. Dong, H. Fang, R. Tai and J. Hu, *J. Synchrotron Radiat.*, 2013, **20**, 413–418.
10 A. Brotchie and X. Zhang, *Soft Matter*, 2010, **7**, 265.
11 X. Zhang, X. Zhang, J. Sun, Z. Zhang, G. Li, H. Fang, X. Xiao, X. Zeng and J. Hu, *Langmuir*, 2007, **23**, 1778–1783.
12 X. Zhang, G. Li, N. Maeda and J. Hu, *Langmuir*, 2006, **22**, 9238–9243.
13 P. G. de Gennes, *Langmuir*, 2002, **18**, 3413–3414.
14 A. Finger and D. Johannsmann, *Phys. Chem. Chem. Phys.*, 2011, **13**, 18015.
15 Y. Wang and B. Bhushan, *Soft Matter*, 2009, **6**, 29.
16 G. Liu and V. S. J. Craig, *ACS Appl. Mater. Interfaces*, 2009, **1**, 481–487.
17 Z. Wu, X. Zhang, X. Zhang, G. Li, J. Sun, Y. Zhang, M. Li and J. Hu, *Surf. Interface Anal.*, 2006, **38**, 990–995.
18 Z. Wu, X. Zhang, X. Zhang, J. Sun, Y. Dong and J. Hu, *Chin. Sci. Bull.*, 2007, **52**, 1913–1919.
19 V. Belova, D. A. Gorin, D. G. Shchukin and H. Möhwald, *Angew. Chem., Int. Ed.*, 2010, **49**, 7129–7133.
20 V. Belova, M. Krasowska, D. Wang, J. Ralston, D. G. Shchukin and H. Möhwald, *Chem. Sci.*, 2012, **4**, 248.
21 S.-T. Lou, Z.-Q. Ouyang, Y. Zhang, X.-J. Li, J. Hu, M.-Q. Li and F.-J. Yang, *J. Vac. Sci. Technol., B: Microelectron. Nanometer Struct.–Process., Meas., Phenom.*, 2000, **18**, 2573.
22 S. Karpitschka, E. Dietrich, J. R. T. Seddon, H. J. W. Zandvliet, D. Lohse and H. Riegler, *Phys. Rev. Lett.*, 2012, **109**, 066102.
23 X. Zhang, D. Y. C. Chan, D. Wang and N. Maeda, *Langmuir*, 2013, **29**, 1017–1023.
24 J. H. Weijs and D. Lohse, *Phys. Rev. Lett.*, 2013, **110**, 054501.
25 Y. Liu and X. Zhang, *J. Chem. Phys.*, 2013, **138**, 014706.
26 H. Peng, M. A. Hampton and A. V. Nguyen, *Langmuir*, 2013, **29**, 6123–6130.
27 B. Borkent, H. Schönherr, G. Le Caër, B. Dollet and D. Lohse, *Phys. Rev. E: Stat., Nonlinear, Soft Matter Phys.*, 2009, **80**, 036315.
28 R. Monchaux, M. Bourgoin and A. Cartellier, *Phys. Fluids*, 2010, **22**, 103304.
29 Y. Tagawa, J. M. Mercado, V. N. Prakash, E. Calzavarini, C. Sun and D. Lohse, *J. Fluid Mech.*, 2012, **693**, 201–215.
30 J. L. Meijering, *Philips Res. Rep.*, 1953, **8**, 270–290.
31 D. Weaire and N. Rivier, *Contemp. Phys.*, 1984, **25**, 59–99.
32 H. Lhuissier and E. Villermaux, *J. Fluid Mech.*, 2013, **714**, 361–392.
33 S. Yang, S. M. Dammer, N. Bremond, H. J. W. Zandvliet, E. S. Kooij and D. Lohse, *Langmuir*, 2007, **23**, 7072–7077.
34 J.-S. Ferenc and Z. Néda, *Phys. A*, 2007, **385**, 518–526.
35 E. N. Gilbert, *Ann. Math. Stat.*, 1962, **33**, 958–972.
36 R. Battino, T. R. Rettich and T. Tominaga, *J. Phys. Chem. Ref. Data*, 1983, **12**, 163–178.
37 R. Battino, T. R. Rettich and T. Tominaga, *J. Phys. Chem. Ref. Data*, 1984, **13**, 563–600.
38 L. Zhang, X. Zhang, Y. Zhang, J. Hu and H. Fang, *Soft Matter*, 2010, **6**, 4515.
39 B. Song, W. Walczyk and H. Schönherr, *Langmuir*, 2011, **27**, 8223–8232.
40 J. H. Weijs, J. H. Snoeijer and D. Lohse, *Phys. Rev. Lett.*, 2012, **108**, 104501.
41 A. Kolmogorov, *The logarithmically normal law of distribution of dimensions of particles when broken into small parts*, NASA-TT-F-12287, 1969.
42 Q. Zhou, C. Sun and K.-Q. Xia, *Phys. Rev. Lett.*, 2007, **98**, 074501.
43 J. Bosbach, S. Weiss and G. Ahlers, *Phys. Rev. Lett.*, 2012, **108**, 054501.
44 F. N. Rhines and B. R. Patterson, *Metall. Trans. A*, 1982, **13**, 985–993.